Micro-Tug-of-War: A Selective Control Mechanism for Magnetic Swimmers

Panayiota Katsamba* and Eric Lauga†

Department of Applied Mathematics and Theoretical Physics, University of Cambridge, Cambridge CB3 0WA, United Kingdom

(Received 4 January 2016; published 30 June 2016)

One of the aspirations for artificial microswimmers is their application in noninvasive medicine. For any practical use, adequate mechanisms enabling control of multiple artificial swimmers will be of paramount importance. Here we theoretically propose a multihelical, freely jointed motor as a selective control mechanism. We show that the nonlinear step-out behavior of a magnetized helix driven by a rotating magnetic field can be exploited when used in conjunction with other helices to obtain a velocity profile that is non-negligible only within a chosen interval of operating frequencies. Specifically, the force balance between the competing opposite-handed helices is tuned to give no net motion at low frequencies (tug-of-war), while in the middle-frequency range, the magnitude and, potentially, the sign of the swimming velocity can be adjusted by varying the driving frequency. We illustrate this idea on a two-helix system and demonstrate how to generalize to N helices, both numerically and theoretically. We then explain how to solve the inverse problem and design an artificial swimmer with an arbitrarily complex velocity vs frequency relationship. We finish by discussing potential experimental implementation.

DOI: 10.1103/PhysRevApplied.5.064019

I. INTRODUCTION

From the beginnings of human intellectual activity, scientists and philosophers have been captivated by the beauty hidden in the smallest scales. Technology has now reached the point where micro- and nanomanipulation are not as elusive as they sounded back in Feynman's 1959 lecture "There's plenty of room at the bottom" [1].

Engineering at the micro- or nanoscale includes challenges beyond the mere miniaturizing process, primarily due to the very physics at these scales [2]. One needs only to zoom down to micrometer resolution and consider something as simple as swimming to appreciate the substantially different physics. In order to self-propel, natural microorganisms need to employ swimming strategies which allow them to go around the constraints set by Purcell's [3] scallop theorem. Examples include the rotation of a helix [4], whose chiral shape couples rotation to translation, as in most bacteria; the propagation of traveling waves along flexible flagella [5,6], as in the spermatozoa of many species; or, the metachronal wave synchronization of a carpet of cilia on ciliated organisms [6–8].

Researchers have proposed and constructed a variety of artificial micro- and nanoswimmers often drawing inspiration from natural swimming methods [9]. These are powered either externally [10], often by magnetic fields, by catalyzing a chemical reaction [11] or from self-phoretic motion [12]. The externally powered swimmers proposed so far include helical propellers [13,14] (illustrated in Fig. 1), motors that use flexible filaments [15–17], and surface walkers [18–21].

Following the success of controlling the motion of single artificial swimmers, realistic applications now demand the possibility for multidevice control [9]. Ideally one would employ the same control inputs to simultaneously move each of these swimmers in a different way or at least to select and move only a subset of them at a time.

Many research groups have manufactured artificial microswimmers that may be selectively controlled. The stress-engineered MEMS microrobot uses an untethered scratch drive actuator and a cantilevered steering arm to move on an electrode-embedded surface [22]. Selective control of multiple robots is achieved by having different snap-down and release voltage pairs for each robot. The Magmite microrobotic platform designed as a system with intrinsic resonance uses pulsed magnetic fields to operate a magnetomechanical spring-mass system on a specialized surface [23]. Selective control is achieved by manufacturing each robot to have a different resonant frequency at which it can be operated. In the Mag-μBot, pulsed external magnetic fields induce a stick-slip motion which results in translation. Electrostatic anchoring on a specialized controlled surface allows selective control among identical robots by preventing motion [24]. Alternatively, selective control can be achieved with an ordinary nonspecialized surface by varying the geometrical and magnetic properties of the robots. This method exploits the fact that for the stick-slip motion, in which the rectangular-shaped robot needs to be lifted on its edge, to be possible, the magnetic torque must exceed the gravitational rest torque [25].

Propellers driven by external oscillating or rotating magnetic fields offer possibilities for simpler selective control strategies that do not require the presence of a

*pa335@cam.ac.uk
†e.lauga@damtp.cam.ac.uk

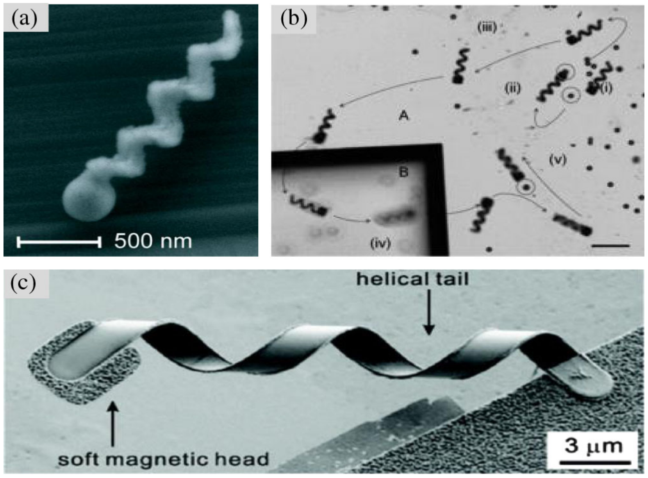

FIG. 1. Experimental realizations of rigid helical swimmers. (a) Chiral silicon dioxide (SiO_2) colloidal propeller. Reprinted (adapted) with permission from A. Ghosh and P. Fischer, Nano Lett. 9, 2243 (2009). Copyright 2009, American Chemical Society. (b) Pick-and-place micromanipulation of a 6-μm-diameter microparticle using a helical swimming micromachine fabricated using 3D direct laser writing from S. Tottori, L. Zhang, F. Qiu, K. K. Krawczyk, A. Franco-Obregn, and B. J. Nelson, Adv. Mater. 24, 811 (2012). Copyright 2012, WILEY-VCH Verlag GmbH & Co. KGaA, Weinheim. (c) SEM of an artificial bacterial flagellum [13] consisting of a ribbonlike helical tail made of a (In, Ga)As/GaAs/Cr trilayer and a soft-magnetic head made of Cr/Ni/Au metal thin films. Reprinted (adapted) with permission from L. Zhang, J. J. Abbott, L. Dong, K. E. Peyer, B. E. Kratochvil, H. Zhang, C. Bergeles, and B. J. Nelson, Nano Lett. 9, 3663 (2009). Copyright 2009, American Chemical Society.

nearby surface. For the achiral three-bead magnetic chain of Ref. [26], altering the field's rotation frequency or strength changes the rotation axis of the microswimmer, giving rise to different modes of motion. Locomotion is only effective for a given range of frequencies of the rotating magnetic field, thus, allowing selective control over geometrically similar microswimmers but with different magnetic properties. Alternatively, one can use the direction of the magnetic moment relative to the long axis of a helical swimmer as a distinguishing control parameter [27]. A multistep algorithm was proposed that allows independent positioning in which oscillating and rotating fields move a selected motor to a certain location while the rest still move, but by the time the selected motor has reached its target, they have returned to their initial positions [27]. Finally, recent work used nanohelices with soft-magnetic bar and cross-shaped heads [28]. The extra magnetization axis in the cross-shaped case allows selective control when two types of external magnetic field rotations are used suitably.

The nonlinear step-out behavior of a magnetized chiral structure such as a helix, or screw, which is driven and guided by an externally applied rotating magnetic field, has been studied [29–34] and proposed as means of providing some selective control [32–34]. When operated below its critical—so-called step-out— frequency, the helix rotates synchronously, phase locked to the rotation rate of the magnetic field, giving rise to a velocity profile which is linear in the operating frequency. At driving frequencies that exceed the step-out frequency, the speed of the helix decays like the inverse power of the driving frequency asymptotically. For a collection of such motors with different step-out frequencies, one can, in theory, switch between modes where all subgroups are operated (for driving frequencies lower than the minimum step-out frequency), to modes with less and less being operated, by adjusting the driving frequency appropriately. However, from a practical standpoint, it is important to be able to selectively control any of the different groups operated, if not simultaneously, at least one at a time, so that they can be allocated to different tasks.

One of the possible applications of artificial microswimmers for which selective control is of paramount importance, is that of noninvasive medicine [9,35], one of the greatest aspirations for nanoscience. Whether they are to access targeted locations in the body to deliver drugs [36], in which case, large numbers of them will be required, or to perform various delicate surgical tasks [37], designing artificial swimmers with adequate multirobot control is of paramount importance. Other important features that the design should encompass are simplicity and robustness so as to cope in complex operating environments and the possibility of speed adjustment by tuning the control parameters. Given the future need for manufacturing large numbers of these motors, it is also important that the fundamental theoretical analysis is undertaken so that the relationship between the design-parameter space and the resulting microswimmer specification be fully understood. These required design features are not all possible for the current strategies.

In this paper, a multihelical, freely jointed motor is proposed and theoretically characterized as a selective control mechanism that encompasses all these desired features. The proposed design arose naturally by considering the main problem of interest. In order to selectively control two motors that use the same method of swimming and are powered by the same external signal, they need to respond differently to it, either because they have some different properties (control via variation in the receiver properties) or because they are manufactured to "listen" only to particular subsignals, e.g., frequencies, that the external signal might consist of (control via distributed signal). Seeking control via variation in the receiver properties is ultimately a quest of systems or methods with an intrinsic nonlinearity in the response of the propellers relative to the control parameter of the external signal. The design needs to have enough degrees of freedom so that the nonlinearity manifests a velocity profile that is non-negligible only within an interval of the control parameter. The control parameter can be the frequency of the driving field, for example. Then for a collection $\{S_1, \ldots, S_N\}$ of N sets of such motors with well-separated effective bands of operational frequencies $\mathcal{B}_n = (\Omega_1^{(n)}, \Omega_2^{(n)})$, if the operating frequency $\omega_h \in \mathcal{B}_n$, the set S_n of robots will be controlled with the rest being stationary or moving at negligible speed.

The nonlinear profile of the single magnetic helix being close to the desired one except for the lack of a cutoff for low driving frequencies has inspired us to add more degrees of freedom and consider a motor that consists of two helices of opposite chirality connected in series, which we call a transchiral (i.e., of different chirality) helical motor. The desired cutoff at low frequencies is established by tuning the force balance between the two opposite-handed helices. In isolation, at low frequencies, the two helices would rotate in the same sense as the magnetic field but translate in opposite directions due to the difference in chirality. Assuming that they are connected by a joint that allows them to freely rotate relative to one another, the helices will pull each other in opposite directions, a competition resembling tug-of-war. The geometric and magnetic characteristics of the two helices can be chosen such that the net motion of the transchiral helical motor is canceled in the low-frequency regime. For the range of frequencies between the two step-out frequencies, the helix with the highest step-out frequency dominates, giving a net velocity profile that monotonically increases from zero to a maximum value, thereby allowing speed adjustment by varying the driving frequency. Finally, above the maximum step-out frequency, there is negligible locomotion.

Adding more degrees of freedom by considering a multihelical motor gives rise to more complex banded velocity profiles with extra features, such as bands of negative velocity that enable reversal of the direction of motion by varying the driving frequency. A simple approximation allows us to solve the inverse problem analytically, and find an algorithm that determines the appropriate design features that would give rise to a prescribed banded velocity profile.

The paper is organized as follows. After reviewing the physics for the step-out velocity profile of a single magnetized helix, we study the mechanics of multibody and multihelical motors. We derive the different velocity profiles attainable by a transchiral and a triple-helical motor. An approximate analytical model is then presented, which allows us to solve the inverse problem of prescribing a banded velocity profile and finding the geometrical design features that give rise to it. We finish by addressing the issue of experimental implementation and sensitivity of our design to experimental errors.

II. DESIGN AND LOCOMOTION OF FIELD-DRIVEN HELICAL SWIMMERS

Magnetized helices guided by a rotating magnetic field can propel effectively in low-Reynolds-number regimes using two physical ingredients. First, just like a compass needle, a permanent magnet subject to an external magnetic field experiences a torque which tends to align its magnetic moment with the external field. If the external field is constantly rotating, it will continuously apply a torque on the object. The second ingredient is due to the low-Reynolds-number fluid dynamics around the helix. Because a helix is chiral, when an external torque is applied to it, it will not only rotate but also translate along its axis at a speed which may be found by computing the full resistance matrix of the helical shape and depends both on its shape and size.

For driving frequencies lower than the step-out frequency, the rotation of the helix is phase locked to that of the field. Above the step-out frequency, however, the helix cannot keep up with the field. The phase difference between the two increases but nonuniformly. During part of the cycle, the helix slowly increases its rotation speed, trying to catch up with the field, then effectively dynamically gives up, slows down, and starts again. The dynamics of a single magnetized helix giving rise to this nonlinear profile is well understood [29–31,33,34,38]. Since the single magnetized helix is the fundamental building block of our proposed device and it is its nonlinear behavior which we wish to exploit for multirobot control, we shall first review its dynamics in detail.

A. Single helix

The notation for the helix is shown in Fig. 2. In the frame of a helix, the geometry of its centerline is parametrized by its arc length $\mathbf{x}$ given by

$$\mathbf{x} = [R\cos(ks\cos\theta), hR\sin(ks\cos\theta), s\cos\theta]. \quad (1)$$

The long axis of the helix is assumed to be aligned with the z axis. The main geometrical characteristics are the following: the helicity index h, which takes the value $+1$ or -1 according to whether the helix is right or left handed, respectively, the angle θ between the local tangent and the helix axis (which is constant), the radius R of the

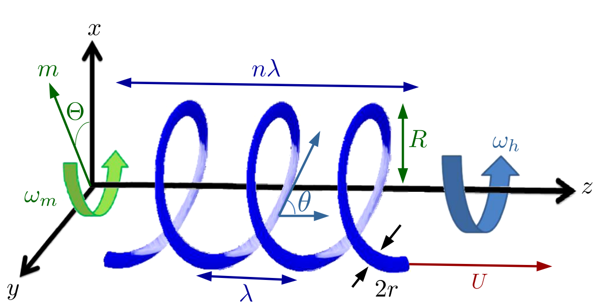

FIG. 2. Geometry of a right-handed helix of wavelength λ, helix angle θ, radius R, diameter of cross section $2r$, and number of wavelengths n. The magnetic field rotates about the z axis with rotation rate ω_h. The helix rotates about the z axis with rotation rate ω_m and translates in the z direction with velocity U.

helical body (i.e., the radius of the cylinder on which the helix is drawn), the radius r of the cross section of the wire (we assume it is a circular cross section), and the number of turns of the helix n. The wave number k of the helix is given by $k = 2\pi/\lambda$, where λ is the wavelength along the helix axis. The values of R, k, and θ are related via the relationship $\cos^2\theta = (1 + R^2k^2)^{-1}$. The arc length along a single turn of the helix is given by $\Lambda = \lambda/\cos\theta$; hence, a helix with n turns will have a total length $\Delta z = n\lambda$ along the z axis and total arc length $\Delta s = n\Lambda = 2\pi nR/\sin\theta$.

The helix is taken to be a permanent magnet, with constant magnetic dipole moment $\mathbf{m}$ which is fixed with respect to the helix geometry and perpendicular to its long axis. We write $|\mathbf{m}| = MV$, where M is the remanent magnetization of the helix, and $V = \pi r^2 \Delta s$ is the volume of the magnetized wire. When placed in an external magnetic field denoted $\mathbf{h}$, it will experience a magnetic torque $\mathbf{T}_m = \mu_0 \mathbf{m} \wedge \mathbf{h}$. If the external magnetic field is rotating about the z axis with angular frequency $\omega_h \mathbf{e}_z$ and assuming that the helix is long enough to not wobble [38], but instead to remain aligned with the z axis, the applied magnetic torque on the helix will also point along the z axis, and the helix will rotate in the x-y plane about the z axis with angular frequency ω_m. If we use Θ to denote the angle between the x axis and $\mathbf{m}$, which rotates with the body, then we have $\omega_m = d\Theta/dt$, and the angle between $\mathbf{m}$ and $\mathbf{h}$ is equal to $\omega_h t - \Theta$, so that we have the torque given by

$$\mathbf{T}_m(t) = \mu_0 |\mathbf{m}||\mathbf{h}| \sin(\omega_h t - \Theta)\mathbf{e}_z. \tag{2}$$

Because of the hydrodynamic rotation-translation coupling property of the helix, it will also translate with velocity U along the z axis.

Resistive-force theory [39,40] may be used to determine the approximate hydrodynamic forces and torques exerted on the helix. In that framework, the force per unit length $\delta\mathbf{f}_{\mathrm{hydr}}$ exerted by the helix on the fluid is given by

$$\delta\mathbf{f}_{\mathrm{hydr}} = c_\perp \mathbf{u} - (c_\perp - c_\parallel)(\mathbf{t}.\mathbf{u})\mathbf{t}, \tag{3}$$

where $\mathbf{u} = U\mathbf{e}_z + \omega_m \mathbf{e}_z \wedge \mathbf{x}$ is the local velocity, and $c_\perp$ and $c_\parallel$ are the resistance coefficients for motion in the directions perpendicular and parallel to the local tangent $\mathbf{t}$ of the centerline. Their ratio $\rho = c_\parallel/c_\perp \approx 1/2$, not being unity, manifests drag anisotropy, which is crucial for propulsion in the zero-Reynolds-number regime [40]. One can obtain the force per unit length exerted by the helix on the fluid along the z axis $\delta\mathbf{f}_{\mathrm{hydr}}.\mathbf{e}_z$, and the torque per unit length $\delta\mathbf{T}_{\mathrm{hydr}} \cdot \mathbf{e}_z = (\mathbf{x} \wedge \delta\mathbf{f}) \cdot \mathbf{e}_z$ exerted by the helix on the fluid along the z axis as

$$\begin{aligned}\delta\mathbf{f}_{\mathrm{hydr}} \cdot \mathbf{e}_z = {} & U(c_\parallel \cos^2\theta + c_\perp \sin^2\theta) \\ & - h(c_\perp - c_\parallel) R\omega_m \sin\theta\cos\theta,\end{aligned} \tag{4}$$

$$\begin{aligned}\delta\mathbf{T}_{\mathrm{hydr}} \cdot \mathbf{e}_z = {} & R^2\omega_m (c_\parallel \sin^2\theta + c_\perp \cos^2\theta) \\ & - h(c_\perp - c_\parallel) RU \sin\theta\cos\theta.\end{aligned} \tag{5}$$

Since these expressions are uniform along the helix, the total force and torque exerted by the helix on the fluid along the z axis are obtained by multiplying the above by the total arc length, i.e., $n\Lambda = 2\pi nR/\sin\theta$.

In the absence of gradients in the external magnetic field, there are no external forces acting on the helix, and, thus, the total hydrodynamic force on the swimmer must be zero, thereby linearly relating U to ω_m. The magnetic torque must balance the hydrodynamic torque exerted by the fluid on the helix due to its motion, leading to the governing equation for the rotation rate.

In its nondimensionalized form, the governing equation for the phase difference between the external field and the helix $\Delta\Theta = \omega_h t - \Theta$ is

$$\frac{d\Delta\Theta}{d\tau} = \frac{\omega_h}{\Omega_{\mathrm{SO}}} - \sin(\Delta\Theta), \tag{6}$$

where Ω_{SO} is the step-out frequency given by

$$\Omega_{\mathrm{SO}} = \frac{\mu_0 |\mathbf{m}||\mathbf{h}|}{c_\perp R^3} \frac{\sin\theta(\rho\cos^2\theta + \sin^2\theta)}{2\pi n\rho}, \tag{7}$$

and τ is the nondimensionalized time, $\tau = \Omega_{\mathrm{SO}} t$.

Equation (6) is the well-known Adler's equation, which, in its more general form, governs the synchronization behavior in a multitude of systems across the spectrum of natural sciences. A simple example in mechanics is the overdamped pendulum driven by a constant torque [41]. More sophisticated systems include the synchronization of the flagella of microorganisms such as *Chlamydomonas* [42], heart pacemaker cells, oscillating neurons, fireflies flashing in unison, and applauding crowds [41,43]. In our case, Eq. (6) captures the synchronization dynamics between the magnetized helix and the driving magnetic field. The phase difference between the two evolves dynamically as a nonuniform oscillator.

The nondimensional time $\Delta\tau$ for the phase difference $\Delta\Theta$ to change by 2π is given by

$$\Delta\tau = \int_0^{2\pi} \left(\frac{d\Delta\Theta}{d\tau}\right)^{-1} d\Delta\Theta. \tag{8}$$

Writing the average angular frequency as $\langle\omega_m\rangle = 2\pi/\Delta\tau$, one obtains

$$\langle\omega_m\rangle = \begin{cases} \omega_h & \text{if } \omega_h \le \Omega_{\mathrm{SO}}, \\ \omega_h[1 - \sqrt{1 - (\Omega_{\mathrm{SO}}/\omega_h)^2}] & \text{if } \omega_h > \Omega_{\mathrm{SO}}. \end{cases} \tag{9}$$

The mean velocity profile being a scalar multiple of $\langle\omega_m\rangle$ follows the same trend, as shown in the top dashed line (black) in Fig. 3 (top curve): It starts off linear and then decays algebraically above the step-out frequency.

B. Multibody motor

Having reviewed the dynamics of a single helix, we now turn to the coupled motion of multiple bodies and show how to exploit and modify this nonlinear step-out profile to the desired banded profile in a more general setting. Consider a motor that consists of N magnetized components that are connected in series along their long axis by joints, so that neighboring magnetized components interact with each other by exerting equal and opposite interaction forces and torques to each other, according to Newton's third law of motion. We assume neighboring magnetized components are at large separations to neglect hydrodynamic interactions (see Sec. II E for a discussion) and that the joint connecting them is negligible in size, not magnetized, and allows free relative rotation about the long axis.

Each component is taken to be a permanent magnet, with magnetic dipole moment $\mathbf{m}_i$ of magnitude $M_i V_i$, where M_i is the remanent magnetization, and V_i is the volume of the magnetized material (no summation convention is used here). The vector $\mathbf{m}_i$ is taken to be fixed and perpendicular to the long axis of the motor.

When placed in an external magnetic field $\mathbf{h}$ rotating with angular velocity $\omega_h \mathbf{e}_z$, each component of the motor will experience a magnetic torque $\mathbf{T}^{(i)}_{\text{magn}} = \mu_0 \mathbf{m}_i \wedge \mathbf{h}$ and will rotate about the z axis with angular frequency ω_{m_i}. As before, we have

$$T^{(i)}_{\text{magn}} = \mu_0 |\mathbf{m}_i||\mathbf{h}| \sin(\omega_h t - \Theta_i)\mathbf{e}_z, \tag{10}$$

where Θ_i is the angle between $\mathbf{m}_i$ and the x axis, and $\omega_h t - \Theta_i$ is the angle between $\mathbf{m}_i$ and $\mathbf{h}$.

In practice, the components we are thinking of, and will consider below, are helices, but there is no reason not to generalize to a general chiral geometry when formulating the kinematics of our multibody motor. Assuming that our magnetized component also translates with velocity U along the z axis, then by linearity, the hydrodynamic forces and torques are related to the velocities and rotation rates as

$$\begin{pmatrix} \mathbf{F}^{(i)}_{\text{hydr}} \\ \mathbf{T}^{(i)}_{\text{hydr}} \end{pmatrix} = \begin{pmatrix} \mathbf{A}^{(i)} & \mathbf{B}^{(i)} \\ \mathbf{B}^{(i)T} & \mathbf{D}^{(i)} \end{pmatrix} \begin{pmatrix} \mathbf{U}^{(i)} \\ \mathbf{\Omega}^{(i)} \end{pmatrix}, \tag{11}$$

where $\mathbf{F}^{(i)}$ and $\mathbf{M}^{(i)}$ are defined as the force and torque that the ith component exerts on the fluid when it is translating at velocity $\mathbf{U}^{(i)} \equiv U\mathbf{e}_z$ common for all components and rotating at angular velocity $\Omega^{(i)}$. Along the z axis, we, thus, have the linear relationships

$$F^{(i)}_{\text{hydr}} = A^{(i)} U + B^{(i)} \frac{d\Theta_i}{dt}, \tag{12}$$

$$T^{(i)}_{\text{hydr}} = B^{(i)} U + D^{(i)} \frac{d\Theta_i}{dt}. \tag{13}$$

The force of interaction between neighboring components is not necessarily zero; however, in the overall force balance, all interaction forces will cancel out and the total force will be zero. Our assumption about the free rotational joint allows us to consider the torque balance for each of the components separately. The system is, thus, subject to

$$\sum_{i=1}^{N} F^{(i)}_{\text{hydr}} = 0, \qquad T^{(i)}_{\text{hydr}} = T^{(i)}_{\text{magn}} \quad \forall i. \tag{14}$$

We proceed by nondimensionalizing the problem. Nondimensional quantities are denoted by hat and nondimensionalized time by τ. Let M be some typical magnetization and V a typical volume of magnetized material and write $M^{(i)} = M\hat{M}^{(i)}$ and $V^{(i)} = V\hat{V}^{(i)}$. Using a typical length scale R and time scale Ω^{-1} given by

$$\Omega = \frac{\mu_0 |\mathbf{h}| M}{c_\perp} \frac{V}{R^3}, \tag{15}$$

we have that $U \sim R\Omega$, $F_{\text{hydr}} \sim c_\perp R^2 \Omega$, $T_{\text{hydr}} \sim c_\perp R^3 \Omega$, hence, $A \sim c_\perp R$, $B \sim c_\perp R^2$, and $D \sim c_\perp R^3$.

The force balance in its nondimensionalized form gives

$$\hat{U} = -\frac{1}{\sum_k \hat{A}^{(k)}} \sum_{j=0}^{N} \hat{B}^{(j)} \frac{d\Theta_j}{d\tau}, \tag{16}$$

where the angles Θ_i obey the coupled dynamics

$$\hat{D}^{(i)} \frac{d\Theta_i}{d\tau} - \frac{\hat{B}^{(i)}}{\sum_k \hat{A}^{(k)}} \sum_{j=1}^{N} \hat{B}^{(j)} \frac{d\Theta_j}{d\tau} = \hat{M}^{(i)} \hat{V}^{(i)} \sin\left(\frac{\omega_h}{\Omega}\tau - \Theta_i\right). \tag{17}$$

This can be written in matrix form as

$$\sum_{k=1}^{N} \alpha_{ik} \frac{d\Theta_k}{d\tau} = \hat{M}^{(i)} \hat{V}^{(i)} \sin\left(\frac{\omega_h}{\Omega}\tau - \Theta_i\right), \tag{18}$$

where the matrix $\boldsymbol{\alpha}$ is defined as

$$\alpha_{ik} = \begin{cases} \hat{D}^{(i)} - \frac{\hat{B}^{(i)2}}{\sum_l \hat{A}^{(l)}} & \text{if } k = i, \\ -\frac{\hat{B}^{(i)}\hat{B}^{(k)}}{\sum_l \hat{A}^{(l)}} & \text{if } k \neq i. \end{cases} \tag{19}$$

C. Multihelical motor

Having formulated our model in terms of a general chiral structure, we now focus on multihelical motors in which the magnetized components are helices.

1. Equations

Let R be a typical helical radius and use this length scale to nondimensionalize the problem, and r a typical radius of the cross section of a filament so that the typical wire volume is $V = \pi r^2 R$. The ith helix has helicity index h_i, angle θ_i, radius $\hat{R}_i R$, wave number n_i, and is made out of a wire of cross-sectional radius $\hat{r}_i r$ and of total nondimensionalized arc length $\Delta\hat{s}_i = 2\pi n_i \hat{R}_i / \sin\theta_i$ and magnetized volume $\hat{V}^{(i)} = \hat{r}_i^2 \Delta\hat{s}_i$. The helix is assumed to have drag coefficient $c_\perp^{(i)} = c_\perp \hat{c}_{\perp_i}$, where $c_\perp$ is a typical resistance coefficient and $\rho_i = c_{\parallel_i}/c_{\perp_i} \approx 1/2$.

For a helix, we can use Eqs. (4) and (5) to directly quote $\hat{A}^{(i)}$, $\hat{B}^{(i)}$, and $\hat{D}^{(i)}$ as

$$\hat{A}^{(i)} = \Delta\hat{s}_i \hat{c}_{\perp_i}(\rho_i \cos^2\theta_i + \sin^2\theta_i), \tag{20}$$

$$\hat{B}^{(i)} = -\Delta\hat{s}_i \hat{R}_i \hat{c}_{\perp_i} h_i (1-\rho_i)\sin\theta_i \cos\theta_i, \tag{21}$$

$$\hat{D}^{(i)} = \Delta\hat{s}_i \hat{R}_i^2 \hat{c}_{\perp_i}(\rho_i \sin^2\theta_i + \cos^2\theta_i). \tag{22}$$

Substituting these into Eq. (16) for a multihelical motor gives

$$\hat{U} = \sum_{j=0}^{N} \mathcal{A}_j \frac{d\Theta_j}{d\tau}, \tag{23}$$

$$\mathcal{A}_j = \frac{\hat{c}_{\perp_j}\Delta\hat{s}_j h_j (1-\rho_j) s_j c_j \hat{R}_j}{\sum_k \hat{c}_{\perp_k}\Delta\hat{s}_k(\rho_k c_k^2 + s_k^2)}, \tag{24}$$

and the matrix $\boldsymbol{\alpha}$ in Eq. (18) is given by

$$\frac{\alpha_{ik}}{\Delta\hat{s}_i} = \begin{cases} \hat{R}_i^2(\rho_i s_i^2 + c_i^2) - h_i(1-\rho_i)s_i c_i \hat{R}_i \mathcal{A}_i, & \text{if } k = i, \\ -h_i(1-\rho_i)s_i c_i \hat{R}_i \mathcal{A}_k, & \text{if } k \neq i. \end{cases} \tag{25}$$

Note that the repeated indices in the above equation do not imply Einstein summation, and we use the shorthand notation $s_i \equiv \sin\theta_i$, $c_i \equiv \cos\theta_i$.

2. Numerical results

The system of N-coupled ordinary differential equations of Eq. (18) can be first solved numerically to obtain the average velocity as a function of the driving frequency. Illustrative results are shown in Fig. 3 in the case of a transchiral motor with two helices, where we pick the parameters $\theta_1 = \theta_2 = \pi/4$, $m_1 = 6$, $m_2 = 3$, $\hat{r}_1 = \hat{r}_2 = 1$, $\hat{R}_1 = \hat{R}_1 = 1$, and show the frequency vs velocity relationship for five different helices characterized by $(n_1, n_2) = (1 - p/4, p/4)$, with $p = \{0, 1, 2, 3, 4\}$. Note that, in principle, the drag coefficients depend on the dimensions of the helices and can, thus, vary; however, the dependence is only logarithmic [39,40] and requires the dimensions of different helices to be orders of magnitude different. We, thus, assume a constant value of the drag coefficients, which is taken out in the nondimensionalization process and take $\hat{c}_{\perp_i} = 1 \forall i$.

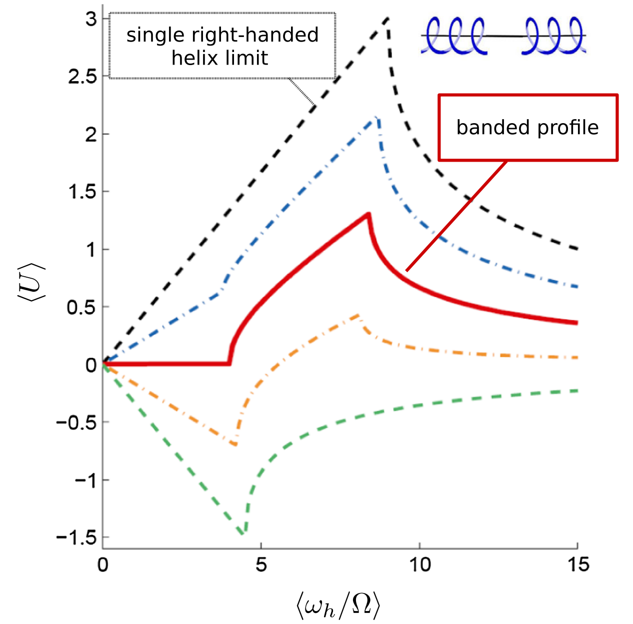

FIG. 3. Mean swimming velocity of two-helix transchiral motor $\langle U \rangle$ as a function of dimensionless frequency ω_h/Ω obtained numerically for the combinations $(n_1, n_2) = (1 - p/4, p/4)$, $p \in 0, 1, 2, 3, 4$. All other parameters are kept fixed: $\theta_1 = \theta_2 = \pi/4$, $\hat{M}_1 = 6$, $\hat{M}_2 = 3$, $\hat{r}_1 = \hat{r}_2 = 1$, and $\hat{R}_1 = \hat{R}_1 = 1$. We observe the transition from the dynamics of a single right-handed helix (top dashed line, black) to that of a single left-handed helix (bottom dashed line, green) via a series of intermediate stages, including the banded profile (middle solid line, red).

Clearly, the addition of one more helix provides extra degrees of freedom for the transchiral motor by altering the standard single-helix step-out profile, and the computational results confirm our original intuition to exploit the competition between the two opposite-handed helices. In Fig. 3, we observe the velocity profile transitions from that of a single right-handed helix (top dashed line, black) to that of a single left-handed helix (bottom dashed line, green), via a series of intermediate stages. In all cases, the swimming speeds always start off proportional to the driving frequency before reaching each of the step-out frequencies consequently. Varying (n_1, n_2) alters the initial slope—most notably, there is a special combination that gives rise to zero slope, and, hence, the banded profile (middle solid line, red). In that case, the transchiral motor has a clear band of operating frequencies outside of which it either does not move (low frequencies) or is very inefficient (high frequencies).

For a triple-helical motor with $(h_1, h_2, h_3) = (+1, -1, +1)$, as shown in Fig. 4, varying the relative dominances of the helices using different combinations for the number of turns n_1, n_2, n_3 gives rise to various velocity profiles, including a banded velocity profile with frequency ranges

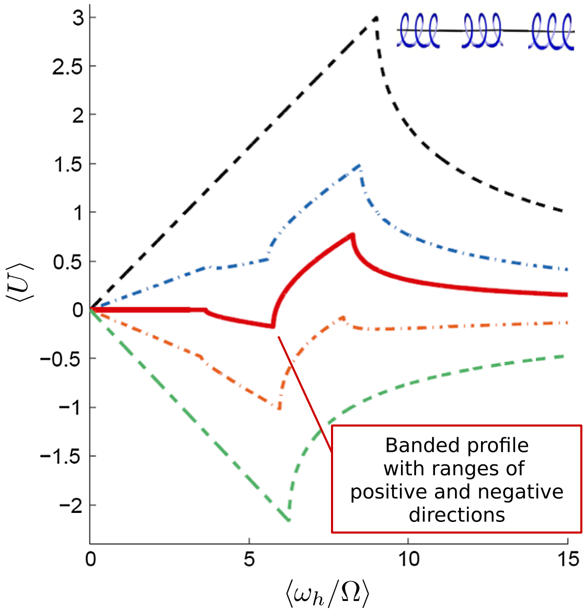

FIG. 4. Propulsion velocity $\langle U \rangle$ as a function of ω_h/Ω obtained numerically for a triple-helical motor with helicities $(h_1, h_2, h_3) = (+1, -1, +1)$ for various combinations of the number of turns, whose values given up to one decimal place are $(n_1, n_2, n_3) = \{(8,0,0), (6,2.8,1), (4,4.2,1), (2,6,1), (0,8,0)\}$ from top to bottom. All other parameters are kept fixed: $(\theta_1, \theta_2, \theta_3) = (\pi/4, \pi/6, \pi/5)$, $(\hat{M}_1, \hat{M}_2, \hat{M}_3) = (6,5,3)$, $\hat{r}_i = 1$, and $\hat{R}_i = 1$ for all i.

with both directionalities (middle solid line, red), thereby allowing reversal of the direction of motion by shifting the driving frequency instead of reversing the direction of rotation of the magnetic field. The general velocity profile for a triple-helical motor has three transition points at which each of the helices steps out with an initial linear increase in the speed before the first transition point and a step-out decay after the last one. The limits of a single, right-handed helix n_2, $n_3 \to 0$ (top dashed line, black) and of a single, left-handed helix n_1, $n_3 \to 0$ (bottom dashed line, green) are also shown.

3. Analytical model

Having characterized our proposed swimmer numerically, we now show how to use a decoupling approximation to model the dynamics analytically, which we will then exploit to theoretically predict the parameter space for motor design.

Inverting Eq. (18), the system of equations takes the form

$$\frac{d\Theta_i}{d\tau} = f_i \sin \Delta\Theta_i + \sum_{j\neq i} I_{ij} \sin \Delta\Theta_j, \tag{26}$$

with I_{ij} the coupling coefficients (note that $I_{ij} = I_{ji}$ since α_{ij} is symmetric). Noting that the off-diagonal components of $\boldsymbol{\alpha}$ are much smaller than the diagonal ones, we approximate α_{ij} as diagonal and neglect the coupling terms. The system of equations then decouples, and we get the approximate system for all values of i,

$$\frac{d\Delta\Theta_i}{d\tau} = \frac{\omega_h}{\Omega} - f_i \sin \Delta\Theta_i, \tag{27}$$

$$f_i = \frac{\hat{M}^{(i)} \hat{r}_i^2}{\hat{R}_i^2(\rho_i s_i^2 + c_i^2) - h_i(1-\rho_i) s_i c_i \hat{R}_i \mathcal{A}_i}, \tag{28}$$

$$\left\langle \frac{d\Theta_i}{d\tau} \right\rangle = \begin{cases} \frac{\omega_h}{\Omega} & \text{if } \omega_h/\Omega < f_i, \\ \frac{\omega_h}{\Omega} - \sqrt{(\frac{\omega_h}{\Omega})^2 - f_i^2} & \text{if } \omega_h/\Omega > f_i, \end{cases} \tag{29}$$

$$= \frac{\omega_h}{\Omega} - \mathbb{1}_{\frac{\omega_h}{\Omega} > f_i} \sqrt{\left(\frac{\omega_h}{\Omega}\right)^2 - f_i^2} \tag{30}$$

$$\langle \hat{U} \rangle = \sum_j \mathcal{A}_j [f - \mathbb{1}_{f > f_j} \sqrt{f^2 - f_j^2}], \tag{31}$$

where $f = \omega_h/\Omega$ is the nondimensional driving frequency, and $\mathbb{1}$ denotes the indicator function ($\mathbb{1}_P$ equals 1 if the statement P is true and 0 otherwise).

Under these assumptions, the phase difference between each helix and the magnetic field obeys the nonuniform oscillator equation Eq. (27) that gives a step-out profile Eq. (29) with a net velocity which is just the linear superposition of the step-out profiles for each of the rotation rates of the helices, Eq. (31). The quantity Ωf_i is the value of ω_h at which the ith helix will step out as part of the multihelical configuration. Importantly, this quantity is different from the step-out frequency for that helix in isolation since all other helices appear in the sum in the denominator of $\mathcal{A}_i$.

Let us now assume that our N helices are numbered in order of increasing values of f_i. Then the behavior of the multihelical motor will be determined by the N transition points $(f_i, \hat{U}_i)$ of the $\langle \hat{U} \rangle$ vs f plot at which the ith helix steps out, where $\hat{U}_i$ is given by

$$\hat{U}_i = \left(\sum_{j=1}^{N} \mathcal{A}_j\right) f_i - \sum_{j<i} \mathcal{A}_j \sqrt{f_i^2 - f_j^2}. \tag{32}$$

The set $\{(f_i, \hat{U}_i)\}$ then fully determines our design-parameter space. Noting that the average nondimensional velocity increases linearly with the operating frequency until we reach the point

$$\left(f_1, \hat{U}_1 = f_1 \sum_{j=1}^{N} \mathcal{A}_j\right) \tag{33}$$

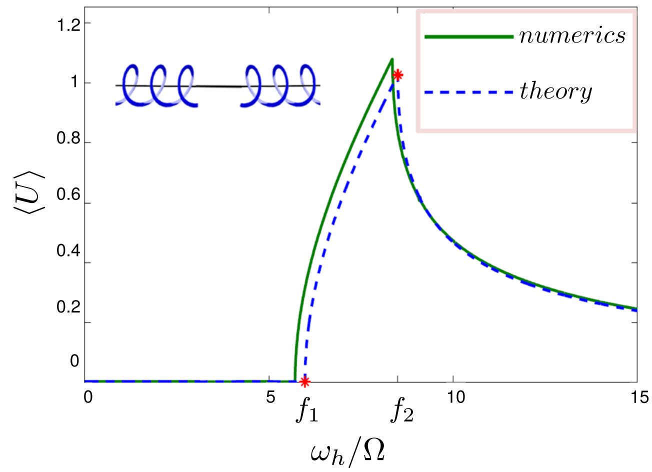

FIG. 5. Mean swimming velocity $\langle U \rangle$ as a function of $f = \omega_h/\Omega$ obtained numerically (solid line, green) and predicted by the theoretical approximation (dashed line, blue) for a double-helical motor designed to have zero net motion at low frequencies. The helical parameters are $\theta_1 = \pi/4$, $\theta_2 = \pi/6$, $n_1 = 6.13$, $n_2 = 5$, $\hat{M}_1 = 6$, $\hat{M}_2 = 5$, $\hat{r}_1 = \hat{r}_2 = 1$, $\hat{R}_1 = \hat{R}_1 = 1$. The two critical frequencies are $f_1 \approx 6$ (with $\hat{U}_1 = 0$) and $f_2 \approx 8.5$ ($\hat{U}_2 \approx 1$).

allows us to choose the geometrical parameters of our helices such that

$$\sum_{j=1}^{N} \mathcal{A}_j = 0. \tag{34}$$

With this choice, the motor stays stationary when operated at frequencies below Ωf_1 and is effectively operated within the band $f \in (f_1, f_N)$ of width $f_N - f_1$. Furthermore, its velocity at the transition points is simply given by

$$\hat{U}_i = -\sum_{j<i} \mathcal{A}_j \sqrt{f_i^2 - f_j^2}. \tag{35}$$

4. Double-helical motor

We illustrate the accuracy of our analytical approach with multihelical motors composed of two and three helices. With two helices, the motor manifests an effective band of frequencies (f_1, f_2) of width $f_2 - f_1$. For $f < f_1$, the artificial swimmer is constructed to be stationary, and for $f \in (f_1, f_2)$, it moves at a speed which increases monotonically with ω_h, whereas above f_2, since both helices have stepped out, it moves at a negligible velocity that decreases as the inverse power of ω_h.

The comparison between the full numerics and the analytical model is shown in Fig. 5. The blue dashed line shows the profile predicted analytically, while the green solid line shows the full computational result without the decoupling approximation. The simple theory is successful at capturing the dynamics of the system and, more important, allows us to construct a design-parameter space for the motor. Indeed, finding the geometrical parameters that give rise to the banded profile is no longer a "tuning" process via repeated numerical simulation. Since we have $\hat{c}_{\perp_j} \approx 1$ and $\rho_j \approx 0.5$ ($j = 1, 2$), one just needs to choose the geometrical parameters so as to satisfy $\mathcal{A}_1 + \mathcal{A}_2 = 0$, which reduces to the simple relationship

$$n_1 \hat{R}_1^2 \cos\theta_1 = n_2 \hat{R}_2^2 \cos\theta_2. \tag{36}$$

Since the denominator in Eq. (28) depends only on n_i, R_i, and θ_i ($i = 1, 2$), for any combination of these that satisfies this criterion, the critical frequencies f_1, f_2 can be readily set to any value by choosing $\hat{M}_i, \hat{r}_i$ accordingly.

5. Triple-helical motor

An additional design feature one might desire is the ability to reverse the direction of motion of the motor by changing the operating frequency alone. This can be achieved with the use of a helical motor composed of three helices. A suitable choice of parameters allows us to split the effective frequency band (f_1, f_3) into two bands $\mathcal{B}_+ = (f_1, f_0)$ and $\mathcal{B}_- = (f_0, f_3)$ of opposite directionality with $\langle \hat{U} \rangle$ positive in $\mathcal{B}_+$ and negative in $\mathcal{B}_-$, where $f_0 \in (f_2, f_3)$ is such that $\langle \hat{U} \rangle|_{f_0} = 0$ and is given by

$$f_0 = \sqrt{\frac{\mathcal{A}_1^2 f_1^2 - \mathcal{A}_2^2 f_2^2}{\mathcal{A}_1^2 - \mathcal{A}_2^2}}. \tag{37}$$

With these choices, the motor is stationary for $f \in (0, f_1)$. Then for $f \in (f_1, f_2)$, it moves in the negative direction, and the speed magnitude increases monotonically from 0 to $|\hat{U}_2|$ as f increases. As f further increases from f_2 to f_3, the velocity increases monotonically from its most negative value $\hat{U}_2$ passing through 0 at f_0, to its most positive value $\hat{U}_3$ at f_3. For f larger than f_3, all three helices step out, giving rise to negligible velocity that decreases as the inverse of f.

The design-parameter space of a triple-helical motor, thus, consists of (a) the boundaries f_1 and f_3 of the effective frequency band, (b) the widths $\Delta f_+ = f_0 - f_1$ and $\Delta f_- = f_3 - f_0$ of the positive and negative bands $\mathcal{B}_+$ and $\mathcal{B}_-$, respectively, and (3) the most negative and most positive velocities $\hat{U}_2$ and $\hat{U}_3$, which occur at f_2 and f_3, respectively.

The parameters $\{\theta_i, n_i, \hat{R}_i, \hat{r}_i, \hat{M}_i\}$ ($1 \le i \le 3$) can be chosen independently and arbitrarily. An example of a velocity profile obtained by choosing parameters suitable to enable two opposite directionality bands is shown in Fig. 6.

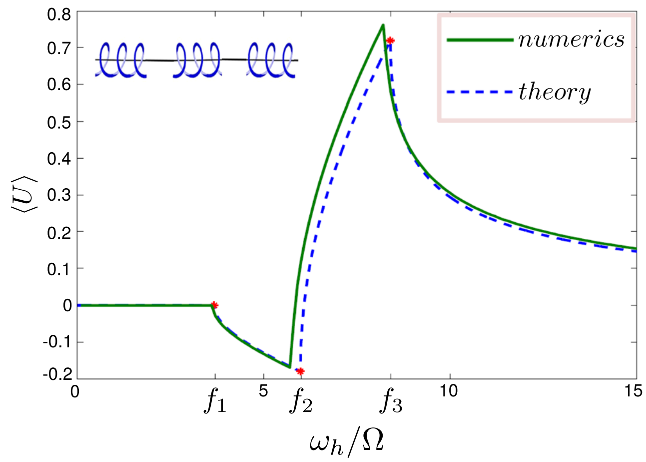

FIG. 6. Mean velocity $\langle U\rangle$ as a function of $f = \omega_h/\Omega$ found numerically (solid line, green) and predicted analytically (dashed line, blue) for a triple-helical motor. The parameters used are $(h_1, h_2, h_3) = (1, -1, 1)$, $(\theta_1, \theta_2, \theta_3) = (\pi/4, \pi/6, \pi/5)$, $(n_1, n_2, n_3) = (4, 4.2, 1)$, $(\hat{M}_1, \hat{M}_2, \hat{M}_3) = (6, 5, 3)$, $\hat{r}_i = \hat{R}_i = 1 \forall i$. The resulting critical points have $(f_1, f_2, f_3) \approx (3.7, 6, 8.4)$ and $(\hat{U}_1, \hat{U}_2, \hat{U}_3) \approx (0, -0.18, 0.72)$.

Here again, the analytical approach compares very favorably with the full numerics.

D. Designing motors with prescribed response functions

An important question for any engineering system is whether it is possible to solve the inverse problem and find the particular design leading to a predetermined response function. In our case, this consists of finding the number of helices N and the values of the parameters $\{\theta_i, n_i, \hat{R}_i, \hat{r}_i, \hat{M}_i\}$ $(1 \le i \le N)$, which will give rise to a given banded velocity profile with $\hat{U}_1 = 0$ and with frequencies of the critical transition points f_i and the corresponding average velocities $\hat{U}_i$ set arbitrarily by the designer. We show below that it is possible to construct a simple algorithm to solve this inverse problem.

For simplicity, we take the helices to all have the same angle $\theta_i = \theta$ and use the approximation $\hat{c}_{\perp_j} \approx 1$, $\rho_j = \rho \approx 0.5$ $(j = 1, 2)$. In the analytical model, expression (24) takes the simpler form

$$\mathcal{A}_j = \frac{h_j \hat{R}_j^2 n_j}{\sum_k \hat{R}_k n_k} \frac{(1-\rho)\sin\theta\cos\theta}{\rho\cos^2\theta + \sin^2\theta}. \tag{38}$$

Noting that the coefficients $\mathcal{A}_i$ are independent of $\hat{M}_i$, whereas the f_i's given in Eq. (28) are linear in $\hat{M}_i$, means that after all the geometrical features are decided, one can always tune the f_i to the desired critical frequencies by choosing the value of $\hat{M}_i$ appropriately. Notably, the expressions for the critical velocities $\hat{U}_i$ given in Eq. (35) involve only the coefficients $\mathcal{A}_j$ with $j < i$ and the values f_i, and, thus, using the chosen values for the f_i's, one can solve for the coefficients $\mathcal{A}_j$ iteratively: the value of $\hat{U}_2$ determines $\mathcal{A}_1$, that of $\hat{U}_3$ determines $\mathcal{A}_2$, etc., until $\hat{U}_N$ which determines $\mathcal{A}_{N-1}$. The iterative formula is given by

$$\mathcal{A}_{l-1} = -\frac{\hat{U}_l + \sum_{k=1}^{l-2} \mathcal{A}_k \sqrt{f_l^2 - f_k^2}}{\sqrt{f_l^2 - f_{l-1}^2}}, \tag{39}$$

for $l = 2, \ldots, N$. Then the value of $\mathcal{A}_N$ is chosen as

$$\mathcal{A}_N = -\sum_{j=1}^{N-1} \mathcal{A}_j \tag{40}$$

in order to satisfy $\hat{U}_1 = 0$. Once the $\mathcal{A}_i$'s are determined, one proceeds to invert the expression in Eq. (38) in order to solve for h_j, $\hat{R}_j$, and n_j. If we choose $n_j \hat{R}_j = a$ for all j's, where a is some constant, then Eq. (38) reduces to

$$\mathcal{A}_j = \frac{h_j \hat{R}_j}{N} \frac{(1-\rho)\sin\theta\cos\theta}{\rho\cos^2\theta + \sin^2\theta}. \tag{41}$$

The helicity indices are given by $h_j = \mathrm{sign}(\mathcal{A}_j)$, so we obtain

$$\hat{R}_j = N|\mathcal{A}_j| \frac{\rho\cos^2\theta + \sin^2\theta}{(1-\rho)\sin\theta\cos\theta}, \qquad n_j = a/\hat{R}_j, \tag{42}$$

and, finally, the values $\hat{M}_i$ are chosen to tune the critical frequencies f_i to the desired values

$$\hat{M}_i = f_i \frac{\hat{R}_i^2(\rho_i s_i^2 + c_i^2) - h_i(1-\rho_i) s_i c_i \hat{R}_i \mathcal{A}_i}{\hat{r}_i^2}. \tag{43}$$

Implementing this algorithm allows the design of almost any banded velocity profile, as demonstrated in Fig. 7. Prescribing the positions of the critical transition points shown as red stars is sufficient to determine the profile shown in solid blue line, which is plotted according to Eq. (23). Most notably, three helices allow for profiles with a banded profile where the last transition point is chosen to have zero velocity, as shown in Fig. 7(a). Such profiles allow a better dropoff of the velocity for higher frequencies compared to that offered by the transchiral motor of Fig. 5. Four helices combine this advantage with the possibility of frequency ranges with motion in the opposite direction [Fig. 7(d)]. With five helices, the crossover frequency between these two ranges can be prescribed [Fig. 7(i)]. Six helices allow for separated positive and negative bands with a prescribed separation [Fig. 7(j)].

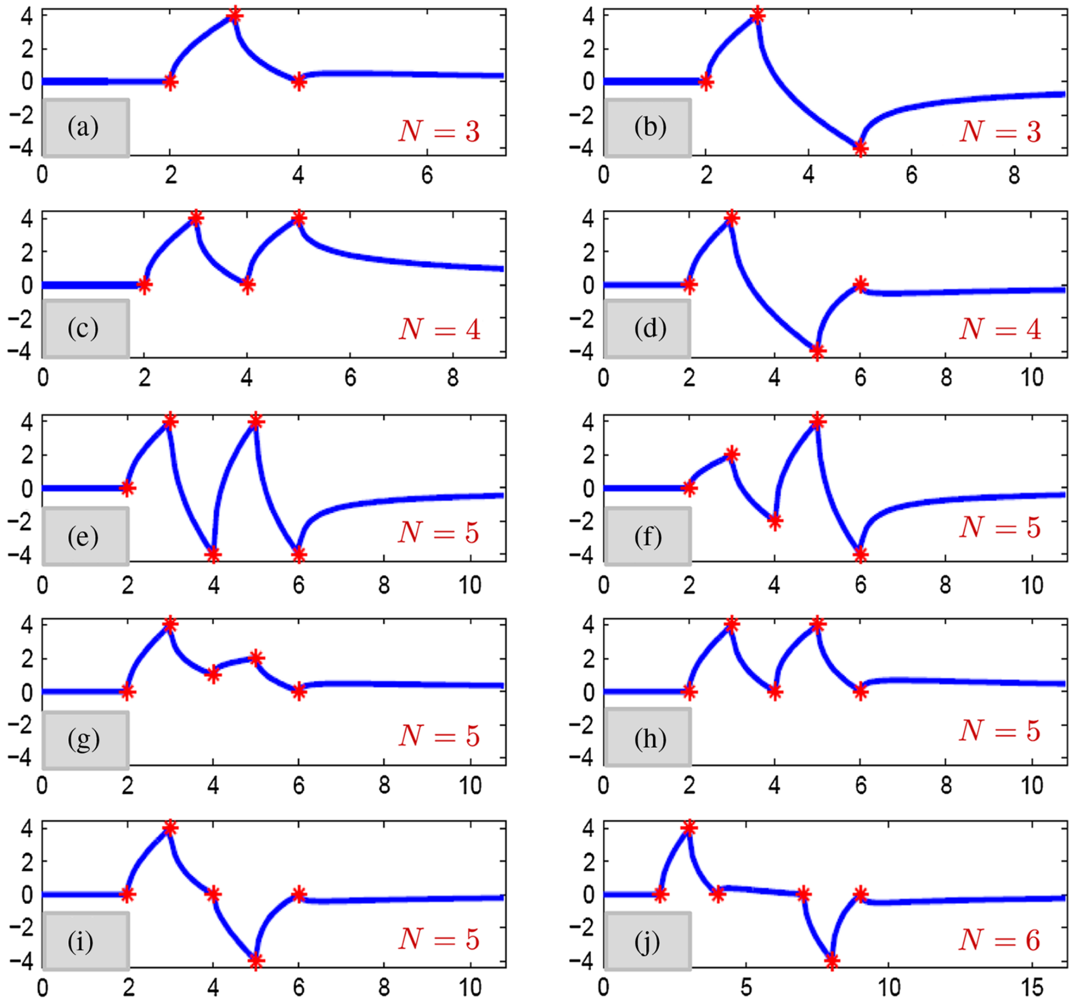

FIG. 7. Various design profiles with $N = 3(\mathrm{a,b}), 4(\mathrm{c,d}), 5(\mathrm{e-i})$ and $6(\mathrm{j})$ helices. The frequencies f_i of the critical transition points shown in red stars and the corresponding average propulsion velocities $\hat{U}_i$ are set arbitrarily by the designer. The design features $\{\theta_i, n_i, \hat{R}_i, \hat{r}_i, \hat{M}_i\}$ $(1 \leq i \leq N)$ are calculated using the analytical algorithm, and the resulting velocity profiles shown as blue solid lines are plotted according to Eq. (23).

E. Experimental considerations

In an experimental setup, the velocity profile of a fabricated multihelical motor varies from the designed theoretical estimates above due to a number of possible effects, including errors during the fabrication process, possible friction from the rotational joint, hydrodynamic interactions between the helical components within it, and thermal fluctuations. In this section, we address these experimental considerations.

1. Hydrodynamic interactions

To discuss some of the implications of hydrodynamic interactions, we now use the setup of a transchiral motor. Consider two helices that are actuated by a rotating magnetic field and coupled via a joint that allows free relative rotation but restricts them to move at the same translational velocity. Assume the two helices are well separated. The effect of the joint is that the two helices push or pull each other and, hence, are not force-free (which would be the case had they not been coupled by the joint). Thus, each of the helices is subject to the far-field velocity of the other as a point force, or Stokeslet, to leading order (had they been decoupled it would have been a rotlet, or point torque). The far field of the first helix at a point with position vector $\mathbf{y}$ relative to the first helix is, thus, given by the Stokeslet term

$$\mathbf{u}_{\mathbf{1}}^{\mathrm{far}} = \frac{1}{8\pi\mu}\left(\frac{\mathbf{1}}{|\mathbf{y}|} + \frac{\mathbf{y}\mathbf{y}}{|\mathbf{y}|^3}\right).\mathbf{F}_{\mathbf{1}}^{\mathrm{hydr}}, \tag{44}$$

where $\mathbf{F}_{\mathbf{1}}^{\mathrm{hydr}}$ is the total hydrodynamic force exerted by helix 1, of total arc length L_1 translating at speed U_1, to the surrounding fluid and scales as $F_1^{\mathrm{hydr}} \sim \mu U_1 L_1$, where μ is the dynamic viscosity of the fluid. Here we assume that the helix is long enough $L_1 \gg R_1$, so as not to wobble [38], or, equivalently, the x, y components of $\mathbf{F}_{\mathbf{1}}^{\mathrm{hydr}}$ to be negligible compared to the z component (the ratio of these scales as

R_1/L_1). The induced far-field flow of helix 1 on helix 2, assuming these are separated by a distance $d \gg R_1, R_2, L_1, L_2$, scales as $u_1^{\rm far}|_2 \sim U_1 L_1/d$. Comparing the velocity field of helix 2 with no hydrodynamic interactions with the far-field velocity acting on it due to helix 1, since $U_1 = U_2$, we obtain

$$\frac{u_1^{\rm far}|_2}{u_2^{\text{no hydro}}} \sim \frac{U_1 L_1/d}{U_2} \sim \frac{L_1}{d}, \tag{45}$$

and similarly for the effect of helix 2 on helix 1, with indices 1 and 2 exchanged. Therefore, the effect of hydrodynamic interactions can be neglected for $d \gg L_1, L_2$.

2. Thermal fluctuations

The issue of thermal fluctuations affects all microswimmers, both biological and manmade. For any solid body actuated by means of an external force $\boldsymbol{F}$ and an external torque $\boldsymbol{T}$ and moving as a result with velocity $\boldsymbol{U}$ and rotation rate Ω given by

$$\begin{pmatrix} \boldsymbol{U} \\ \Omega \end{pmatrix} = \begin{pmatrix} \boldsymbol{\mathcal{M}} & \boldsymbol{\mathcal{N}} \\ \boldsymbol{\mathcal{N}}^T & \boldsymbol{\mathcal{O}} \end{pmatrix} \begin{pmatrix} \boldsymbol{F} \\ \boldsymbol{T} \end{pmatrix}, \tag{46}$$

the mobility matrix above [which is the inverse of the matrix in Eq. (11)] also governs the diffusive behavior of the body via the fluctuation-dissipation theorem. Assuming thermal equilibrium at temperature T, the translational diffusion constant of a solid body is given by the Stokes-Einstein relationship $\boldsymbol{D} = k_B T \boldsymbol{\mathcal{M}}$, where k_B is the Boltzmann constant, while the rotational diffusion constant is given by $\boldsymbol{D_R} = k_B T \boldsymbol{\mathcal{O}}$. For a body with a typical length scale L, the constituent submatrices $[\mathcal{M}]$, $[\mathcal{N}]$, $[\mathcal{O}]$ of the mobility matrix scale as $[\mathcal{M}] \sim (\mu L)^{-1}$, $[\mathcal{N}] \sim (\mu L^2)^{-1}$, $[\mathcal{O}] \sim (\mu L^3)^{-1}$ [40].

Comparing the typical time scales for diffusion-induced motion $\tau_D \sim L^2/[D]$ and diffusion-induced reorientation $\tau_R \sim 1/[D_R]$ [40] with the locomotion-induced time scales for translation $\tau_{\rm trans} \sim L/U$ and rotation $\tau_{\rm rot} \sim 1/\omega$, the two ratios of time scales, which have to be small for thermal fluctuations to be neglected, are

$$\frac{\tau_{\rm trans}}{\tau_D} \sim \frac{k_B T}{\mu L^2 U}, \qquad \frac{\tau_{\rm rot}}{\tau_R} \sim \frac{k_B T}{\mu L^3 \omega}. \tag{47}$$

At room temperature, $k_B T \sim 10^{-21} J$; taking the dynamic viscosity of water $\mu \sim 10^{-3}$ Pa s and a typical frequency of 10 Hz, if we wish these ratios to be of the order of 10^{-2} or 10^{-3}, the motors need to be a few micrometers in size, which is consistent with the size used in current experimental implementations.

3. Collection of motors and fabrication errors

Let us now investigate the effect of fabrication errors, i.e., the fact that the equipment produces motors with errors in their design features, and illustrate how robust the velocity profiles are to such errors.

Assume that one attempted to fabricate a collection of 100 identical multihelical motors with given geometrical and magnetic features. Such a process is prone to experimental error; hence, as the driving frequency is varied, each motor follows a slightly perturbed velocity profile. Hence, if one designs a multihelical motor to obtain a given velocity profile and fabricates one such motor with his equipment giving rise to a 5% error to each of the design features of the motor, the actual velocity profile will deviate from the designed one.

As an indication of this variation, we simulate this numerically by considering 100 realizations of the same design, where the values for the design features are drawn from a Gaussian distribution with mean μ equal to the designed value and standard deviation σ given by $3\sigma = 0.05 \times \mu$. In order to make this choice, we have used the fact that for the Gaussian distribution, the values less than 3 standard deviations away from the mean account for 99.73% of the set. The designed parameters, were taken to have the following values, shown to one decimal place: $(h_1, h_2, h_3) = (1, -1, 1)$, $(n_1, n_2, n_3) = (4, 9.3, 6.5)$, $(\theta_1, \theta_2, \theta_3) = (\pi/4, \pi/6, \pi/5)$, $(\hat{M}_1, \hat{M}_2, \hat{M}_3) = (18, 9, 4.1)$, $\hat{r}_i = 1$, and $\hat{R}_i = 1$ for all i.

Ensemble averages of the velocity give us an idea of the deviations from the designed profile a realistic realization would have. The average velocity of each of these 100 motors for various frequencies is shown in Fig. 8. The velocities of 100 motors drawn from the same Gaussian distribution at a given frequency will have the designed velocity as their mean. Because of variations from the mean, the velocity of an individual propeller can have direction opposite to the expected one, especially for frequencies for which the designed speed is close to zero, as shown in Figs. 8(a), 8(b), and 8(d). However, the important theoretical design features are conserved under noisy conditions, and with an increase in the frequency, the swimmers undergo the transitions in the magnitude of the velocity: small → negative → small → positive → small. The idea proposed in this paper should, thus, be experimentally robust as far as fabrication errors are concerned.

4. Joints

The basic ingredient of our proposed mechanism is the competition between the two opposite-handed helices, and it requires relative rotation between the helices, possibly with friction. A nonzero rotational friction will perturb the velocity profiles (hence, we have assumed a friction-free rotational joint for simplicity), but it will not modify the basic physical ideas proposed above. As elusive as they might sound, setups with low rotational friction already

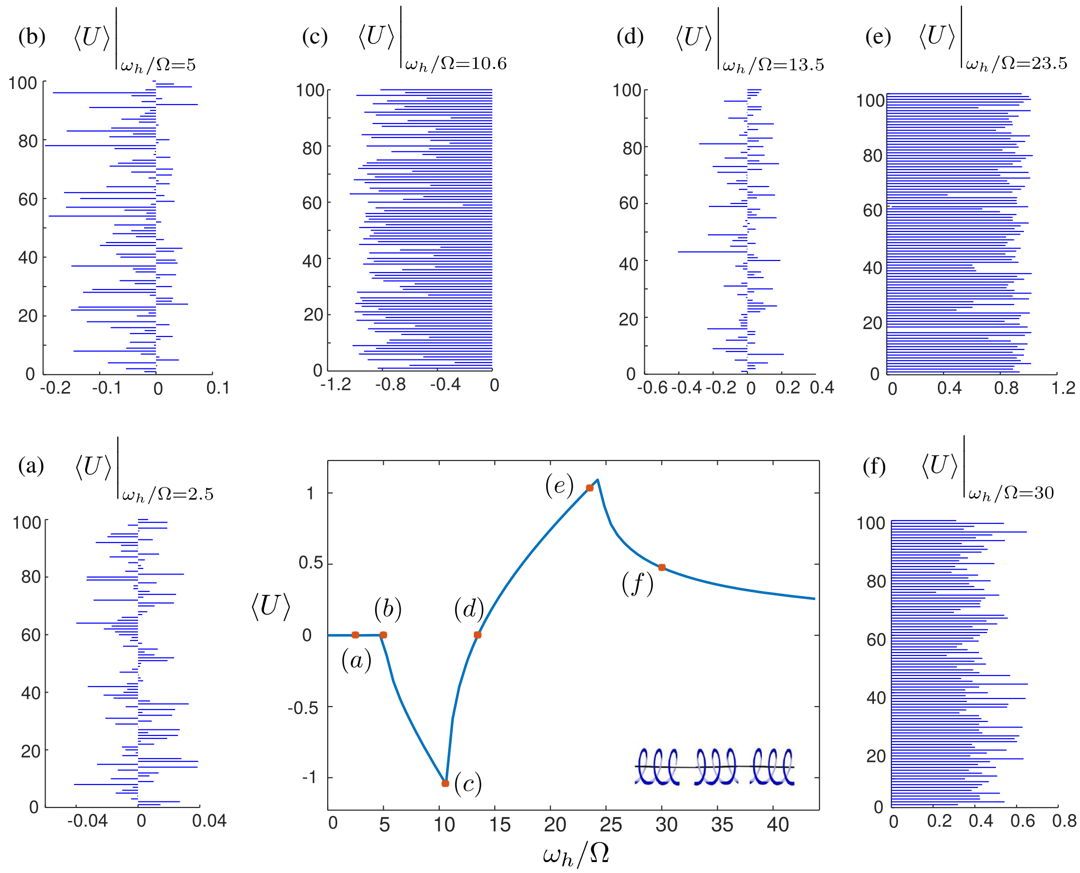

FIG. 8. Simulation of an experiment with experimental errors: The velocities of 100 motors drawn from the same Gaussian distribution with mean μ equal to the designed value and standard deviation σ given by $3\sigma = 0.05 \times \mu$. The designed parameters, were taken to have the following values, shown to one decimal place: $(h_1, h_2, h_3) = (1, -1, 1)$, $(n_1, n_2, n_3) = (4, 9.3, 6.5)$, $(\theta_1, \theta_2, \theta_3) = (\pi/4, \pi/6, \pi/5)$, $(\hat{M}_1, \hat{M}_2, \hat{M}_3) = (18, 9, 4.1)$, $\hat{r}_i = 1$, $\hat{R}_i = 1$ for all i. The important theoretical design features are conserved under noisy conditions and with an increase in the frequency the swimmers undergo the transitions in the magnitude of the velocity: small (a,b) → negative (c) → small (d) → positive (e) → small (f).

exist in nature, even below the nanometer scale. In molecules, single and triple covalent bonds, e.g., between carbon atoms, do allow free rotation of the parts of the molecule on either side of the bond if there are no steric hindrance problems. Perhaps electrostatic interactions between dipole-charged helices can be used to set up an equilibrium distance between them, from which they can rotate relative to each other without contact. Alternatively, one could use a modified version of the "Christmas" cracker setup of Ref. [44]. In that context, boron-nitride nanotubes of different radii with their ends overlapping exhibit ultrahigh interlayer friction. Graphene sheets, on the other hand, have extremely low friction when sliding past each other [45]. A hybrid design with nanotubes that have frictional anisotropy in rotation (easy) and translation (difficult) could be a practical solution.

III. CONCLUSION

This paper addresses the problem of selective control of multiple artificial swimmers. We began by identifying the need for a design with a suitable intrinsic nonlinearity such that each device can function only within a given band of frequencies. Adding more degrees of freedom by extending the single helix to the multihelical, freely jointed motor proposed here, enabled us to exploit the step-out feature to obtain the desired velocity profile.

The velocity profile for a single helix increases linearly with the rotation rate of the magnetic field until it reaches the step-out frequency, after which it decays. In our multihelical motor, choosing the magnetization and geometric parameters suitably, net motion can be canceled for sufficiently low operating frequencies (micro-tug-of-war) whereas in the high-frequency regime where all the helices have stepped out, motion is negligible. In the middle-frequency range, velocity increases monotonically with the driving frequency for the transchiral case. The added degrees of freedom of the triple-helical motor can be used so that the direction of motion can also be reversed by altering the frequency within the effective band.

A simple approximation enables us to construct a design-parameter space to obtain analytical estimates of our design's resulting features. Most notably, these relations are simple enough so that a simple algorithm can be employed to solve the inverse problem: We can choose prior to experimental fabrication or numerical simulation the geometric and magnetic parameters of the design that will give rise to the desired banded velocity profile, which we design by prescribing the transition points. With enough helices, we have enough degrees of freedom to prescribe a banded velocity profile with "forward" and "reverse" frequency bands of widths and separation of our choice.

As theorists, we have introduced in this paper the idea of achieving a selective control mechanism using mechanical principles alone. By tuning the mechanical balance between competing helices we use their nonlinear step out behaviours to compose the desired velocity profile. We hope that these ideas, along with our discussion on experimental constraints and how to limit them, will motivate experimental groups to develop practical realizations of the transchiral helical motor.

ACKNOWLEDGMENTS

This work is funded in part by the European Union through a Marie Curie CIG Grant (E. L.) and by the EPSRC (P. K.).

[1] R. P. Feynman, There's plenty of room at the bottom (data storage), J. Microelectromech. Syst. **1**, 60 (1992).

[2] M. Wautelet, Scaling laws in the macro-, micro- and nanoworlds, Eur. J. Phys. **22**, 601 (2001).

[3] E. M. Purcell, Life at low Reynolds number, Am. J. Phys. **45**, 3 (1977).

[4] L. Turner, W. S. Ryu, and H. C. Berg, Real-time imaging of fluorescent flagellar filaments, J. Bacteriol. **182**, 2793 (2000).

[5] D. Bray, *Cell Movements* (Garland, New York, 2000).

[6] C. Brennen and H. Winet, Fluid mechanics of propulsion by cilia and flagella, Annu. Rev. Fluid Mech. **9**, 339 (1977).

[7] I. R. Gibbons, Cilia and flagella of eukaryotes, J. Cell Biol. **91**, 107s (1981).

[8] M. A. Sleigh, J. R. Blake, and N. Liron, The propulsion of mucus by cilia, Am. Rev. Respir. Dis. **137**, 726 (1988).

[9] B. J. Nelson, I. K. Kaliakatsos, and J. J. Abbott, Microrobots for minimally invasive medicine, Annu. Rev. Biomed. Eng. **12**, 55 (2010).

[10] S. J. Ebbens and J. R. Howse, In pursuit of propulsion at the nanoscale, Soft Matter **6**, 726 (2010).

[11] W. F. Paxton, K. C. Kistler, C. C. Olmeda, A. Sen, S. K. St. Angelo, Y. Cao, T. E. Mallouk, P. E. Lammert, and V. H. Crespi, Catalytic nanomotors: Autonomous movement of striped nanorods, J. Am. Chem. Soc. **126**, 13424 (2004).

[12] R. Golestanian, T. B. Liverpool, and A. Ajdari, Designing phoretic micro- and nano-swimmers, New J. Phys. **9**, 126 (2007).

[13] L. Zhang, J. J. Abbott, L. Dong, K. E. Peyer, B. E. Kratochvil, H. Zhang, C. Bergeles, and B. J. Nelson, Characterizing the swimming properties of artificial bacterial flagella, Nano Lett. **9**, 3663 (2009).

[14] A. Ghosh and P. Fischer, Controlled propulsion of artificial magnetic nanostructured propellers, Nano Lett. **9**, 2243 (2009).

[15] R. Dreyfus, J. Baudry, M. L. Roper, M. Fermigier, H. A. Stone, and J. Bibette, Microscopic artificial swimmers, Nature (London) **437**, 862 (2005).

[16] W. Gao, S. Sattayasamitsathit, K. M Manesh, D. Weihs, and J. Wang, Magnetically powered flexible metal nanowire motors, J. Am. Chem. Soc. **132**, 14403 (2010).

[17] O. S. Pak, W. Gao, J. Wang, and E. Lauga, High-speed propulsion of flexible nanowire motors: Theory and experiments, Soft Matter **7**, 8169 (2011).

[18] P. Tierno, R. Golestanian, I. Pagonabarraga, and F. Sagués, Controlled Swimming in Confined Fluids of Magnetically Actuated Colloidal Rotors, Phys. Rev. Lett. **101**, 218304 (2008).

[19] P. Tierno, O. Güell, F. Sagués, R. Golestanian, and I. Pagonabarraga, Controlled propulsion in viscous fluids of magnetically actuated colloidal doublets, Phys. Rev. E **81**, 011402 (2010).

[20] C. E. Sing, L. Schmid, M. F. Schneider, T. Franke, and A. Alexander-Katz, Controlled surface-induced flows from the motion of self-assembled colloidal walkers, Proc. Natl. Acad. Sci. U.S.A. **107**, 535 (2010).

[21] L. Zhang, T. Petit, Y. Lu, B. E. Kratochvil, K. E. Peyer, R. Pei, J. Lou, and B. J. Nelson, Controlled propulsion and cargo transport of rotating nickel nanowires near a patterned solid surface, ACS Nano **4**, 6228 (2010).

[22] B. R. Donald, C. G. Levey, and I. Paprotny, Planar microassembly by parallel actuation of MEMS microrobots, J. Microelectromech. Syst. **17**, 789 (2008).

[23] D. R. Frutiger, K. Vollmers, B. E. Kratochvil, and B. J. Nelson, Small, fast, and under control: Wireless resonant magnetic micro-agents, International Journal of Robotics Research **29**, 613 (2010).

[24] C. Pawashe, S. Floyd, and M. Sitti, Multiple magnetic microrobot control using electrostatic anchoring, Appl. Phys. Lett. **94**, 164108 (2009).

[25] S. Floyd, E. Diller, C. Pawashe, and M. Sitti, Control methodologies for a heterogeneous group of untethered magnetic micro-robots, International Journal of Robotics Research **30**, 1553 (2011).

[26] U. K. Cheang, F. Meshkati, D. Kim, M. J. Kim, and H. C. Fu, Multiple-robot drug delivery strategy through coordinated teams of microswimmers, Appl. Phys. Lett. **105**, 083705 (2014).

[27] P. Mandal, V. Chopra, and A. Ghosh, Independent positioning of magnetic nanomotors, ACS Nano **9**, 4717 (2015).

[28] S. Tottori, N. Sugita, R. Kometani, S. Ishihara, and M. Mitsuishi, Selective control method for multiple magnetic helical microrobots, J. Micro-Nano Mech. **6**, 89 (2011).

[29] E. J. Smith, D. Makarov, S. Sanchez, V. M. Fomin, and O. G. Schmidt, Magnetic Microhelix Coil Structures, Phys. Rev. Lett. **107**, 097204 (2011).

[30] V. M. Fomin, E. J. Smith, D. Makarov, S. Sanchez, and O. G. Schmidt, Dynamics of radial-magnetized microhelix coils, Phys. Rev. B **84**, 174303 (2011).

[31] V. M. Fomin, E. J. Smith, D. D. Karnaushenko, D. Makarov, and O. G. Schmidt, Asymmetric drag in oscillatory motion: Ratchet effect without an asymmetric potential, Phys. Rev. E **87**, 052122 (2013).

[32] M. Ishiyama, M. Sendoh, and K. I. Arai, Magnetic micromachines for medical applications, J. Magn. Magn. Mater. **41**, 242 (2002).

[33] B. H. McNaughton, K. A. Kehbein, J. N. Anker, and R. Kopelman, Sudden breakdown in linear response of a rotationally driven magnetic microparticle and application to physical and chemical microsensing, J. Phys. Chem. B **110**, 18958 (2006).

[34] A. W. Mahoney, N. D. Nelson, K. E. Peyer, B. J. Nelson, and J. J. Abbott, Behavior of rotating magnetic microrobots above the step-out frequency with application to control of multi-microrobot systems, Appl. Phys. Lett. **104**, 144101 (2014).

[35] M. Sitti, Miniature devices: Voyage of the microrobots, Nature (London) **458**, 1121 (2009).

[36] W. Gao, D. Kagan, O. S. Pak, C. Clawson, S. Campuzano, E. Chuluun-Erdene, E. Shipton, E. E. Fullerton, L. Zhang, E. Lauga, and J. Wang, Cargo-towing fuel-free magnetic nanoswimmers for targeted drug delivery, Small **8**, 460 (2012).

[37] F. Ullrich, C. Bergeles, J. Pokki, O. Ergeneman, S. Erni, G. Chatzipirpiridis, S. Pan, C. Framme, and B. J. Nelson, Mobility experiments with microrobots for minimally invasive intraocular surgery, Invest. Ophthalmol. Visual Sci. **54**, 2853 (2013).

[38] Y. Man and E. Lauga, The wobbling-to-swimming transition of rotated helices, Phys. Fluids **25**, 071904 (2013).

[39] J. Gray and G. J. Hancock, The propulsion of sea-urchin spermatozoa, J. Exp. Biol. **32**, 802 (1955).

[40] E. Lauga and T. R. Powers, The hydrodynamics of swimming microorganisms, Rep. Prog. Phys. **72**, 096601 (2009).

[41] S. H. Strogatz, *Nonlinear Dynamics and Chaos* (Westview Press, Cambridge, MA, 2000).

[42] K. Y. Wan, R. E. Goldstein, and K. C. Leptos, Lag, lock, sync, slip: The many phases, of coupled flagella, J. R. Soc. Interface **11**, 20131160 (2014).

[43] A. Pikovski, M. Rosenblum, and J. Kurths, *Synchronization, A Universal Concept in Nonlinear Sciences* (Cambridge University Press, Cambridge, England, 2001).

[44] A. Nigus, A. Siria, P. Vincent, P. Poncharal, and L. Bocquet, Ultrahigh interlayer friction in multiwalled boron nitride nanotubes, Nat. Mater. **13**, 688 (2014).

[45] M. Dienwiebel, G. S. Verhoeven, N. Pradeep, J. W. M. Frenken, J. A. Heimberg, and H. W. Zandbergen, Superlubricity of Graphite, Phys. Rev. Lett. **92**, 126101 (2004).